J Nondestruct Eval
DOI 10.1007/s10921-012-0131-2

Acoustic Emission Sensor Calibration for Absolute Source Measurements

Gregory C. McLaskey · Steven D. Glaser

Received: 24 August 2011 / Accepted: 17 January 2012

Abstract This paper describes sensor calibration and signal analysis techniques applicable to the method of acoustic emission (AE) and ultrasonic testing. They are particularly useful for obtaining absolute measurements of AE wave amplitude and shape, which can be used to constrain the physics and mechanics of the AE source. We illustrate how to perform calibration tests on a thick plate and how to implement two different mechanical calibration sources: ball impact and glass capillary fracture. In this way, the instrument response function can be estimated from theory, without the need for a reference transducer. We demonstrate the methodology by comparing calibration results for four different piezoelectric acoustic emission sensors: Physical Acoustics (PAC) PAC R15, PAC NANO30, DigitalWave B1025, and the Glaser-type conical sensor. From the results of these tests, sensor aperture effects are quantified and the accuracy of calibration source models is verified. Finally, this paper describes how the effects of the sensor can be modeled using an autoregressive-moving average (ARMA) model, and how this technique can be used to effectively remove sensor-induced distortion so that a displacement time history can be retrieved from recorded signals.

Keywords Deconvolution · Green's function · Time domain modeling · Transfer function

G.C. McLaskey (✉) · S.D. Glaser
Department of Civil and Environmental Engineering, University of California, 621A Sutardja Dai Hall (CITRIS Building), Berkeley, CA 94720-1758, USA
e-mail: gmclaskey@berkeley.edu

S.D. Glaser
e-mail: glaser@berkeley.edu

Published online: 26 January 2012

1 Introduction

Nondestructive evaluation techniques, such as ultrasonic testing and the method of acoustic emission (AE), use signals recorded from piezoelectric sensors to detect surface vibrations and gain information about a material or structure [1, 2]. These signals are a function of source effects, wave propagation effects, and instrumentation effects, as described schematically in Fig. 1. To isolate and better understand the source or wave propagation, the effects of the sensor and recording system must be characterized. Specifically, we would like to know the precise physical quantity (displacement, velocity, etc.) to which the recorded signal is most closely related and quantify any distortion that the sensor or recording system imparts to the signal. We refer to this characterization as sensor calibration.

In many cases, researchers do not need to calibrate their sensing instruments because measurements are based on arbitrarily defined signal thresholds or the relative timing of wave arrivals. Alternatively, researchers may wish to quantitatively evaluate the absolute amplitude of recorded waves or discern the time history or shape of the waves emanating from the wave source. This information can be used to identify the strength and time history of the forces or moments associated with the wave source in order to constrain the physical mechanisms involved (i.e. grain crushing, tensile fracture, shear slip, piezoelectric pulse, etc.). (See [3, 4], for example.) Additionally, absolute sensor calibration enables researchers to quantitatively compare their results with others and advance the collective understanding of the physics and mechanics of AE and other stress wave sources, which will lead to improved, traceable nondestructive evaluation techniques.

As illustrated in Fig. 1, the sequence of events which lead to a recorded signal can be separated into a number of dis-

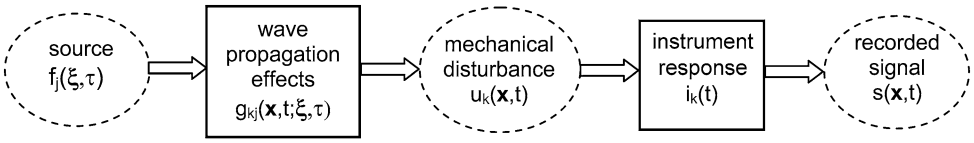

Fig. 1 Block diagram of the sequence of events linking the source to the recorded signal

tinct processes. In order to calibrate a sensor, both the input and output of the *instrument response* box, shown in Fig. 1, must be calculated or measured, so that the effects of the sensor and recording system can be isolated from the wave propagation and source effects. This is accomplished by comparing the recorded signal, $s(\mathbf{x}, t)$, to the precise mechanical disturbance (e.g. the displacement, velocity, acceleration, strain) that produced the signal. Here we describe the disturbance as displacement, $u_k(\mathbf{x}, t)$, a quantity that is either measured with an independently calibrated sensor (a reference sensor), or is calculated from theory. In many cases a reference sensor is not available, is not sensitive enough, or must be calibrated itself. Therefore, we describe the procedure for sensor calibration against theoretical calculations.

An alternative category of calibration, reciprocity calibration, utilizes the "reversible" nature of most piezoelectric sensors: they can be used as both a transmitter and receiver, see e.g. [5–7]. (Reciprocity calibration does not work with newer sensors with built-in matching preamp, e.g. DigitalWave (DW) B1025LD, and Physical Acoustics PAC-R15-AST.) A detailed discussion of reciprocity calibration is beyond the scope of the current paper.

The mathematical and conceptual framework upon which the current calibration approach relies is described in Sect. 2. Section 3 discusses calibration sources and focuses on two different mechanical sources of stress waves used for calibration: ball impact and glass capillary fracture. Section 4 describes the characterization of wave propagation effects, using the elastodynamic Green's function. The estimation of the instrument response function in the frequency domain is then demonstrated in Sect. 5. Lastly, we describe a convenient method for modeling the instrument response function in the time domain. This time domain model can be used to simulate the sensor's distorting effects, or to remove the sensor effects from the recorded signals.

For the purposes of case study and example, we tested four different types of AE sensors on a 50 mm thick steel plate. The four sensors are the Glaser-type conical piezoelectric sensor, e.g. [3, 4, 8, 9], the Physical Acoustics (PAC) PAC R15, the PAC NANO30, and the DigitalWave (DW) B1025. The Glaser-type sensor is a laboratory-standard, wide-band displacement sensor (see Sect. 5.2), and the other three are widely used commercial sensors. The PAC R15 is a general purpose 150 kHz resonant sensor. The PAC NANO30 is described as a miniature sensor with nominal operating frequency of 270–970 kHz. The DigitalWave B1025 is a wideband sensor with a nominal operating bandwidth from 100 kHz to 3 MHz. Though we focus our attention on AE sensors and analysis techniques for the characterization of AE sources, the methodology is valid for a wide variety of sensors common to the stress wave nondestructive testing methods such as impact-echo [10] and ultrasonic techniques which operate in the frequency range of ~10 kHz to ~4 MHz.

2 Theoretical Framework

The physics of wave propagation and transduction are extremely complicated. Instead of attempting to account for every detail, we cast our analysis into a simplified and idealized framework. This framework establishes the operating assumptions or rules by which mathematical and conceptual models operate. In this paper, we present signal analysis and sensor calibration schemes based on a transfer function framework [6, 11], which relies on a Green's function formalism [12, 13]. While this framework relies on some assumptions, stated below, it acts as a starting point from which problems can be posed and models can be tested.

Though all sensors have a finite aperture or sensing area over which physical measurements are averaged in some way, it is initially assumed that each sensor is essentially a point receiver, and that recorded signals are proportional to the wave field sampled at a single location, denoted $\mathbf{x}$. Any distortions due to sensor aperture are simply treated as errors that cause the sensor response to diverge from the ideal case of a point receiver. Likewise, the calibration sources described in Sect. 3 are also assumed to act at point locations. The point-source and point-receiver assumptions simply imply that the source and sensor act on regions which are small compared to the wavelengths of interest. In many cases this is a valid assumption. These assumptions allow us to use a single Green's function for calibration and analysis. Alternatively, To and Glaser [14] demonstrated the technique of integrating over multiple Green's functions for finite source or finite sensor problems.

The transfer function framework relies on the assumption that both the wave propagation effects and the instrument response (the two boxes in Fig. 1) can be modeled as linear, time invariant systems (see, for example [15]). In the context of AE and ultrasonics, this means that the materials and sensors behave the same today as they will tomorrow, and that signal amplitudes are directly proportional to source amplitudes if the frequency content and location of the source

does not change. Under these assumptions, wave propagation effects can be mathematically described as a convolution with the appropriate Green's function, and the effects of the sensor and recording system can be described as a convolution with the instrument response function. In this work, we treat the entire recording system (i.e. the sensor, cables, any preamplifiers, and the data recorder) as a single system which is described by the instrument response function. Alternatively, each subcomponent could be characterized separately. Because we employ a linear transfer function approach, nonlinear details such as instrument saturation must be treated as exceptions to these rules.

Following Fig. 1, the signal recorded from a sensor at location $\mathbf{x}$ can be expressed as

$$s(\mathbf{x},t) = u_k(\mathbf{x},t) * i_k(t) = f_j(\boldsymbol{\xi},\tau) * g_{kj}(\mathbf{x},t;\boldsymbol{\xi},\tau) * i_k(t). \tag{1}$$

In this and subsequent equations, $*$ represents convolution, $f_j(\boldsymbol{\xi},\tau)$ is the force acting in the j direction at location $\boldsymbol{\xi}$ that the source imposes on the test specimen, $g_{kj}(\mathbf{x},t;\boldsymbol{\xi},\tau)$ is the elastodynamic Green's function which describes the displacement in the k direction at point $\mathbf{x}$ and time t due to a unit impulsive force at location $\boldsymbol{\xi}$ in the direction j at time τ [13]; $i_k(t)$ is the instrument response function in the k direction which is to be determined in a calibration test.

Alternatively, if we wish to characterize the source with a set of self-equilibrating forces, such as those from a source buried within a specimen (as is typical in AE tests), the force vector $f_j(\boldsymbol{\xi},\tau)$ can be replaced with a moment tensor $m_{jp}(\boldsymbol{\xi},\tau)$. In this case, the recorded signal can be expressed as

$$\begin{aligned} s(\mathbf{x},t) &= u_k(\mathbf{x},t) * i_k(t) \\ &= m_{jp}(\boldsymbol{\xi},\tau) * g_{kj,p}(\mathbf{x},t;\boldsymbol{\xi},\tau) * i_k(t), \end{aligned} \tag{2}$$

where $g_{kj,p}(\mathbf{x},t;\boldsymbol{\xi},\tau)$ is the first spatial derivative of the elastodynamic Green's function in the p direction. Regardless of how the source is characterized, the role of the instrument response function $i_k(t)$ remains the same. Therefore, for the calibration of an AE sensor, the calibration source need not be representative of a real AE source, but it must produce stress waves in the appropriate frequency range. In this work, we employ (1) because the calibration sources used in this study apply forces on the surface of the specimen. In the above formulation, knowledge of the Green's function, $g_{kj}(\mathbf{x},t;\boldsymbol{\xi},\tau)$, and instrument response function, $i_k(t)$, is sufficient to completely characterize the wave propagation and instrumentation effects, respectively.

In a calibration test, the recorded signal, $s(\mathbf{x},t)$, is compared to a theoretically calculated mechanical disturbance. In this work, we choose to compare recorded signals to calculated displacement time history

$$u_k(\mathbf{x},t) = f_j(\boldsymbol{\xi},\tau) * g_{kj}(\mathbf{x},t;\boldsymbol{\xi},\tau). \tag{3}$$

Alternatively, velocity, acceleration, and strain could be substituted, and can be derived from spatial or temporal derivatives of $u_k(\mathbf{x},t)$. We refer to $u_k(\mathbf{x},t)$ as the 'theoretical signal' because it is the specimen displacement in the i direction which should theoretically exist at the sensor location $\mathbf{x}$ on the calibration test specimen due to the forcing function $f_j(\xi,\tau)$ of the calibration source. The instrument response function $i_k(t)$ can be found by deconvolving (3) from (1):

$$\begin{aligned} i_k(t) &= s(\mathbf{x},t) * u_k(\mathbf{x},t)^{-1} \\ &= s(t) * f_j(\boldsymbol{\xi},\tau)^{-1} * g_{kj}(\mathbf{x},t;\boldsymbol{\xi},\tau)^{-1}. \end{aligned} \tag{4}$$

This is most easily achieved in the frequency domain:

$$\begin{aligned} I_k(\omega) &= S(\mathbf{x},\omega)/U_k(\mathbf{x},\omega) \\ &= S(\mathbf{x},\omega)/[F_j(\boldsymbol{\xi},\varpi)G_{kj}(\mathbf{x},\omega;\boldsymbol{\xi},\varpi)], \end{aligned} \tag{5}$$

where $I_k(\omega)$, $S(\mathbf{x},\omega)$, $U_k(\mathbf{x},\omega)$, $F_j(\boldsymbol{\xi},\varpi)$, and $G_{kj}(\mathbf{x},\omega;\boldsymbol{\xi},\varpi)$ are the temporal Fourier transforms of $i_k(t)$, $s(\mathbf{x},t)$, $u_k(\mathbf{x},t)$, $f_j(\boldsymbol{\xi},\tau)$, and $g_{kj}(\mathbf{x},t;\boldsymbol{\xi},\tau)$, respectively. To calculate $I(\omega)$ in this way, we must first obtain an experiment-theory pair: $s(t)$ and $u_k(\mathbf{x},t)$, so an experiment must be designed such that motions felt by the sensor under consideration are very well modeled by the theoretical signal, $u_k(\mathbf{x},t)$. This is achieved by employing a calibration source which is modeled by a known forcing function $f_j(\boldsymbol{\xi},\tau)$, and conducting the experiment on a specimen for which the wave propagation effects can be modeled by a known or easily computed Green's function $g_{kj}(\mathbf{x},t;\boldsymbol{\xi},\tau)$.

3 Calibration Sources

In order to determine the instrument response function $i_k(t)$, we must have a known source, $f_j(\boldsymbol{\xi},\tau)$, which produces vibrations of known amplitude and shape. An ideal calibration source imposes a unidirectional force, acts on a region which is small in size (in order to satisfy the point source approximation), introduces waves with a broad range of frequencies into the test specimen, and has a smooth frequency spectrum over the entire frequency range for which the calibration is to be valid. Example sources can be found in [16].

Mechanical sources such as pencil lead break [17], capillary fracture [18], and impact [3, 9, 19], are ideal because they are intuitively simple, and the forces they introduce to a specimen are directly linked to physically meaningful, directly measurable quantities. These sources are impulsive or step-like, so they are very broadband in frequency, and their short temporal duration results in ideal waveforms for straightforward identification of the various wave phases (P waves, S waves, etc.). This paper focuses on two different, well characterized, mechanical sources which can be used for absolute sensor calibration: ball impact and glass capillary fracture.

Alternatively, electromechanical sources generated from capacitive and piezoelectric transducers offer excellent repeatability and are easily automated. The difficulty with electromechanical sources is that the precise electromechanical properties of the transducer are complicated and are typically unknown to the user. In order to precisely model the forces that the transducer imposes on the specimen, the source transducer itself must be well characterized: the instrument response, coupling effects, and radiation pattern must all be considered. Piezoelectric transducers themselves are often resonant and are therefore incapable of producing short duration pulses or steps without ringing or distortion [14]. Consequently, we suggest using transducer sources only for relative calibration.

Thermo-mechanical sources excite stress waves in a material by rapid localized heating of a specimen via a pulsed laser, electric arc, or some other form of electromagnetic radiation [20]. These sources hold many of the same advantages as electromechanical sources—repeatability and easy automation—but suffer from the same drawback: because of their extremely complicated physics, they have not yet been characterized to the level of the two mechanical sources described below.

3.1 Glass Capillary Fracture

When conducting a calibration test using a glass capillary fracture, a short (∼2 mm) length of thin walled glass capillary tube is laid on its side and slowly loaded in the direction perpendicular to the specimen face until it fractures. We suggest loading the capillary with a small blunt object such as a 2 mm diameter metal cylinder rather than a razor blade. The loading cylinder is oriented with its axis parallel to the surface of the test block but perpendicular to the axis of the capillary tube. Capillary diameter is typically 100 to 400 µm, and under these conditions it typically breaks at a force of 5–25 N. When the capillary fractures, the surface unloads very rapidly. The force time history, $f(t)$, that the capillary fracture imposes on the test specimen is very nearly equal to a step function with a rise time (unload time), $t_{\text{rise}} < 200$ ns [16, 18], though t_{rise} has some dependence on the size of the capillary [3]. This source has been used by many researchers because the force at which the fracture occurs, f_{amp}, is equal to the amplitude of the step, and can be independently measured for absolute calibration. The capillary-break forcing function can be modeled as

$$\begin{aligned} f(t) &= f_{\text{amp}}/2 * (1 - \cos(\pi t/t_{\text{rise}})) && 0 \le |t| \le t_{\text{rise}}, \\ f(t) &= 0 && t < 0, \\ f(t) &= f_{\text{amp}} && t > t_{\text{rise}}. \end{aligned} \tag{6}$$

The force time function and its spectrum are shown in Fig. 2a and 2b, respectively. Typically, t_{rise} is very small and results in a frequency bandwidth that is much greater than that of the calibrated sensor. Therefore the exact value of t_{rise} and the precise form of (6) are unimportant.

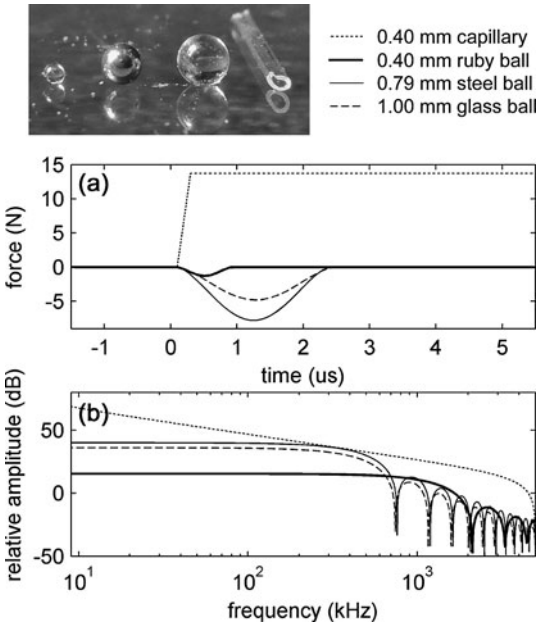

Fig. 2 Force time functions (**a**) and corresponding frequency spectra (**b**) (estimated from (6) and (7)) for a glass capillary fracture calibration source and the impact of balls of various sizes and materials dropped 310 mm onto the surface of a 50 mm thick steel plate

3.2 Ball Impact

For a ball impact calibration test, a small (∼1 mm) diameter ball is dropped onto the test specimen. In these tests, the ball is typically dropped through a small hole in a platform of known height (from fingers or from a fine sponge) down a tall, ∼40 mm diameter clear plastic tube. The platform improves repeatability, and the tube prevents the ball from being lost on subsequent bounces. The impact imposes an impulse-like force. The precise forcing function, $f(t)$, that the ball imparts to the test specimen can be calculated from Hertzian theory [3, 19], and is well modeled by

$$\begin{aligned} f(t) &= f_{\max} \sin(\pi t/t_c)^{3/2} && 0 \le |t| \le t_c, \\ f(t) &= 0 && \text{otherwise}, \end{aligned} \tag{7}$$

where $t_c = 4.53(4\rho_1\pi(\delta_1 + \delta_2)/3)^{2/5} R_1 v_0^{-1/5}$ is the time the ball spends in contact with the specimen, and the maximum force $f_{\max} = 1.917\rho_1^{3/5}(\delta_1 + \delta_2)^{-2/5} R_1^2 v_0^{6/5}$. In preceding equations, $\delta_i = (1 - \mu_i^2)/(\pi E_i)$, and E and μ are the Young's modulus and Poisson's ratio, respectively. R_1 and v_0 are the radius and incoming velocity of the ball. Subscript 1 refers to the material of the ball and subscript 2 refers to the material of the test specimen. The change in momentum that the ball imparts to the test specimen, equal to the area under the force time function $f(t)$, can be independently calculated based on the mass of the ball and the rebound height [3]. Equation (7) is only strictly valid if the ball bounces back to the same height as it was dropped, but as an approximation, if the ball bounces back to only half

its original height, then the peak force $f_{\max 1/2} \approx 0.75 f_{\max}$. By using balls of various sizes and different drop heights, the ball source offers variability in amplitude and frequency content.

Three different types of balls were used for the calibration tests described in this paper: a 1.00 mm diameter glass ball, a 0.79 mm diameter steel ball, and a 0.40 mm diameter ruby ball, pictured in Fig. 2. Forcing functions, calculated from (7), for the impact of these three balls when dropped 310 mm onto a 50 mm thick steel plate, are shown in Fig. 2a compared with the forcing function for a glass capillary fracture (6) with measured $f_{\text{amp}} = 14$ N and t_{rise} assumed to be 200 ns. The ruby ball produces a pulse ~1 µs in duration; the steel and glass balls produce pulses with a nearly identical ~2.3 µs duration, but different amplitudes.

The amplitude of the Fourier transform of these source functions are shown in Fig. 2b. As shown, the spectrum of the ball source is flat at low frequencies and consists of a series of lobes which are separated by zeros at higher frequencies. The zeros in the spectrum of the ball source make the calculation of $i_k(t)$ at these high frequencies particularly challenging, therefore calibrations which use the ball source are typically only assumed to be valid for frequencies below $0.85 f_{\text{zero}} \approx 1.5/t_c$, where f_{zero} is the frequency of the first zero.

3.3 Source Repeatability

Though the glass capillary source is quite repeatable, some small spectral variations can be observed (4 dB/MHz from 0.5–1.5 MHz) [3]. This variability is likely due to small differences in the wall thickness and localized flaws in the glass. The ball impact source is extremely repeatable. Small variations in the rebound height of the ball produce negligible variations in this source. Occasionally, the ball may hit a piece of dust or a surface irregularity which saps the ball's kinetic energy and causes a significant reduction in the ball's rebound height as well as somewhat abnormal stress waves [3]. Each calibration test reported in this paper was repeated five times, but rather than plotting averages of the five calibration tests (which may include some significant outliers), each of the time series and spectra shown in this paper (Figs. 5–9) are from single calibration tests which exhibited, "normal" or non-outlier behavior.

4 Test Geometry and Green's Functions

An ideal test specimen for primary, i.e. absolute, calibration is one for which wave propagation can be well modeled. The geometry should be simple and the specimen made from a material which allows high frequency stress waves to propagate without excess attenuation or scattering. Thick plates of aluminum, steel, glass, and poly(methyl methacrylate) (PMMA) can all be used as effective test specimens. Previous calibration studies [3, 6] have shown that while the absolute sensitivity of a piezoelectric sensor can vary by an order of magnitude when coupled to different materials (presumably due to the differing acoustic impedance), the shape of $I(\omega)$ does not change dramatically. Thus, it may be possible to transfer calibration results from one material to another, as long as absolute sensitivity is scaled appropriately.

Attenuation in PMMA is significant at higher frequencies (>500 kHz for ~50 mm propagation distances) and should be estimated and modeled (e.g. following To and Glaser [14]). In the other materials mentioned, attenuation was shown to have negligible effect on recorded waves for the frequency range/propagation distances described in this study [3]. When studying wave propagation in rock or concrete, scattering of elastic waves may be non-negligible and will add another layer of complexity to wave propagation models.

Greens functions can be calculated analytically for only a few geometries such as an infinite whole space and a half space [13, 21, 22]. For other specimen geometries, numerical models such as finite element or finite difference codes can be employed, but the calculation of Green's functions in this way is difficult because high frequencies require small grid spacing and low frequencies require a long time duration. Green's functions used in this study were calculated with a computer program [23] which uses a generalized ray theory approach. These Green's functions were then verified against theoretical solutions [22, 24, 25] and finite element models [9].

AE and ultrasonic sources cause disturbances both normal and tangential to the surface where the sensor is mounted. In the general case, a sensor will respond differently to displacements in different directions, but the vast majority of AE sensors are predominantly sensitive to surface normal motion (the 3 direction in Fig. 3), therefore we assume $i_1(t) = 0$, $i_2(t) = 0$, and $i_3(t) = i(t)$, and calibrate the sensor response against the surface normal component of displacement, $u_3(\mathbf{x}, t)$. Additionally, both the ball impact and capillary fracture calibration sources impose forces which act at location ξ, in the 3 direction, therefore only the

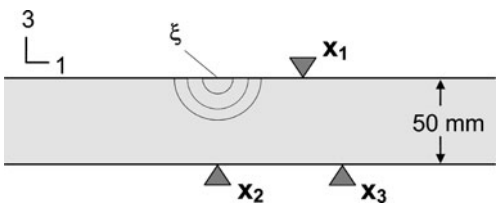

Fig. 3 Experimental setup for the calibration tests on a thick plate. Three different sensor test positions relative to the location of the source, $\boldsymbol{\xi}$, are shown

Green's function, g_{33}, is needed, and (4)–(5) reduce to the scalar equations:

$$i(t) = i_3(t) = s(\mathbf{x}, t) * u_3(\mathbf{x}, t)^{-1} = s(t) * f_3(\boldsymbol{\xi}, \tau)^{-1} * g_{33}(\mathbf{x}, t; \boldsymbol{\xi}, \tau)^{-1}, \quad (8)$$

$$I(\omega) = I_3(\omega) = S(\mathbf{x}, \omega)/U_3(\mathbf{x}, \omega) = S(\mathbf{x}, \omega)/[F_3(\boldsymbol{\xi}, \varpi)G_{33}(\mathbf{x}, \omega; \boldsymbol{\xi}, \varpi)]. \quad (9)$$

If, instead, we wished to calibrate a shear sensor that is sensitive to motions in the 1 direction, we would need the Green's function g_{13}.

The calibration tests described below were performed on a 50 mm thick steel plate, 610 mm square. All sensors were coupled to the specimen surface with Sonotech ultrasonics gel shear couplant. The sensors were held in place with a sensor holder made from a fixed acrylic plastic plate which contains a threaded hole for the Glaser-type sensor and press-fit holes of the appropriate sizes for the three commercial sensors. A single exemplar of each model was used for all experiments.

Three sensor positions relative to the location of the calibration source are shown in Fig. 3. Position 1 ($\mathbf{x_1}$) is a surface location on the same side of the test block as the source and 45 mm away. The largest signal to noise ratio is typically achieved in Position 1 due to the presence of the Rayleigh wave, and the spectrum of the Position 1 Green's function is typically smoother than those of Positions 2 and 3, as shown in Fig. 4d. Position 2 ($\mathbf{x_2}$) is the epicentral location, directly beneath the source. At this location all displacements are in the plate normal direction and the aperture effect is minimized. Additionally, the g_{33} Green's function for Position 2 is insensitive to small changes in the source or sensor locations. Position 3 ($\mathbf{x_3}$) is an off-epicenter location for which the wave displacements are at an oblique angle from the surface normal. Sensors in Position 3 will see both a P wave and a large S wave.

Note that true Green's functions have units of pm/N/s and are inconvenient to sketch. Therefore, Fig. 4 shows calculated ground displacements for the three sensor positions, obtained from the convolution of the Green's functions $g_{33}(\mathbf{x}_1, t; \boldsymbol{\xi}, \tau)$, $g_{33}(\mathbf{x}_2, t; \boldsymbol{\xi}, \tau)$, and $g_{33}(\mathbf{x}_3, t; \boldsymbol{\xi}, \tau)$ with the force time function for the 400 µm ruby ball impact shown in Fig. 2.

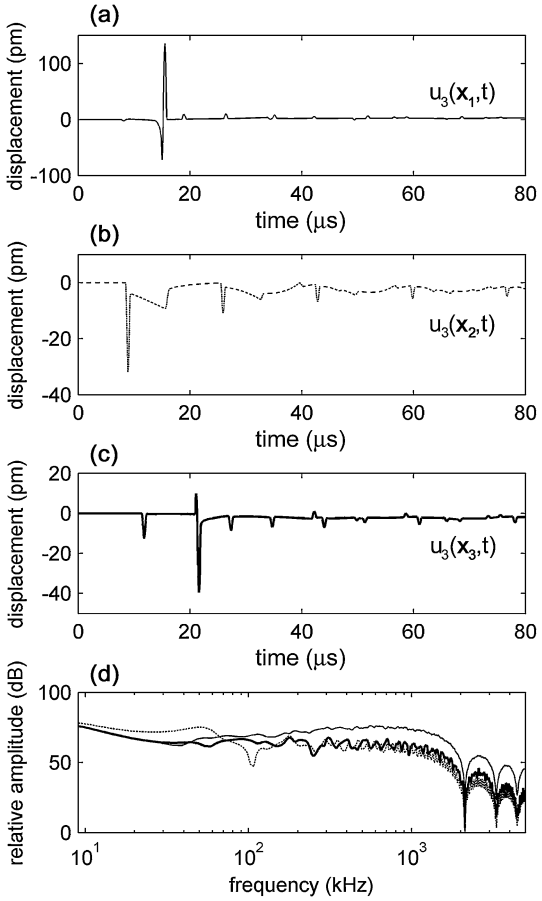

Fig. 4 Theoretical displacements in the 3 direction, $u_3(\mathbf{x}_1, t)$, $u_3(\mathbf{x}_2, t)$, and $u_3(\mathbf{x}_3, t)$, for the three sensor positions shown in Fig. 3. These synthetic signals are calculated by convolving the source function for a 0.40 mm ruby ball dropped 310 mm onto a 50 mm thick steel plate with the appropriate Green's functions for three different sensor positions. (**a**) Displacements felt at Position 1, which is 45 mm away from the source and on the same side of the plate as the source, include a small amplitude P-wave, which arrives before a large amplitude Rayleigh wave, and small amplitude PP, PS, PPPP, PPPS, etc. reflections. (**b**) Displacements felt at Position 2, which is located directly beneath the source, through the thickness of the plate, are characterized by a large amplitude initial P-wave arrival, a ramp in displacement resulting from the near-field component of the displacement field, and a number of evenly spaced reflections (PPP, PPPPP, PPPPPPP, etc.) through the thickness of the plate. (**c**) Displacements felt at Position 3, which is offset 64 mm from Position 2, are characterized by a moderate-sized P wave and a strong S wave immediately preceded by a converted evanescent wave, which has opposite polarity. (**d**) The amplitude of the Fourier transform of these three synthetic signals. The zeros in the spectra at approximately 2.2, 3.3, and 4.4 MHz are the result of the 0.40 mm ruby ball source function, which is common to all three signals, while the fine, tooth-like roughness of the spectra, particularly apparent in the $u_3(\mathbf{x}_2, t)$, and $u_3(\mathbf{x}_3, t)$ results below 1 MHz, arise from the Green's functions

5 Instrument Response in the Frequency Domain

This section describes how the instrument response function can be estimated by simple spectral division. Once a well-characterized calibration source and suitable Green's function for a particular sensor location have been found, a calibration experiment must be conducted so that an experiment-theory input-output signal pair, $s(\mathbf{x}, t)$ and $u_3(\mathbf{x}, t)$, is obtained. Instrument response is then directly estimated from (9). Examples of $s(\mathbf{x}_1,t)$ and $u_3(\mathbf{x}_1,t)$ are shown in Fig. 5 for Position 1 on the 50 mm thick steel test plate and a glass capillary fracture was used as a common source for all four sensors tested. The theoretical signal, $u_3(\mathbf{x}_1,t)$,

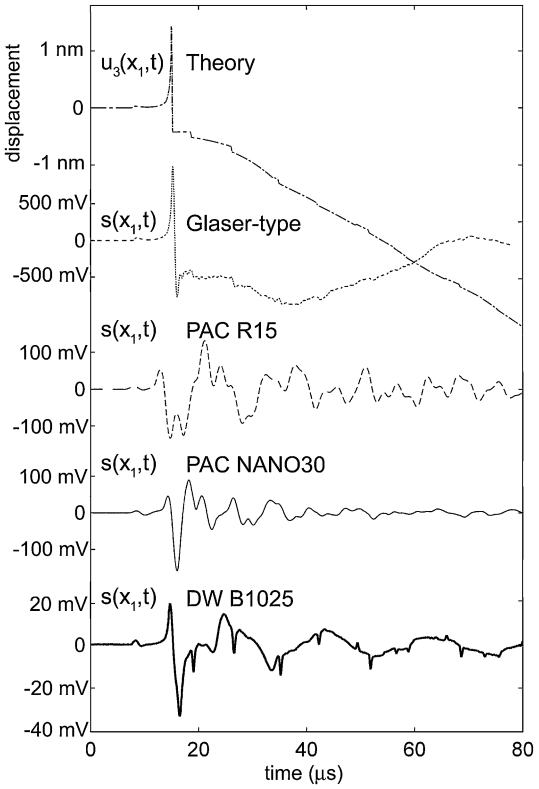

Fig. 5 Experiment-theory pairs from a calibration test in sensor Position 1 on a 50 mm thick steel plate, and a 0.40 mm glass capillary calibration source. The top trace is the theoretical signal calculated from (3). The second through fifth traces are recorded signals in response to a single glass capillary fracture source, simultaneously recorded by each of the four sensors tested: Glaser-type, PAC R15, PAC NANO30, and DW B1025, respectively. Each of the four sensors have identical source-sensor geometry and measure mechanical disturbances from the same glass capillary source, so any differences in recorded signals are attributed to instrument response distortions

is calculated from (3) using $g_{33}(\mathbf{x}_1, t; \boldsymbol{\xi}, \tau)$, while $f_3(\boldsymbol{\xi}, \tau)$ was calculated from (6). In other tests, the ball impact source was used and $f_3(\boldsymbol{\xi}, \tau)$ was calculated from (7).

Once $s(\mathbf{x}, t)$ and $u_3(\mathbf{x}, t)$ are obtained, each signal is Fourier transformed in an identical fashion, and spectral ratios are taken. Figure 6a shows the amplitude of the Fourier transform (FT) of the signals shown in Fig. 5. All signals were digitized at 10 MHz, windowed with a 400 μs Blackman Harris window centered on the first wave arrival, and Fourier transformed with the fast Fourier transform (FFT) algorithm. Following (9), $S(\mathbf{x}, \omega)$ is divided by $U_3(\mathbf{x}, \omega)$ at each Fourier frequency to obtain $\hat{I}(\omega)$, which is an estimate of the true instrument response spectrum, $I(\omega)$. The amplitude and phase of $\hat{I}(\omega)$ are shown in Fig. 6c and 6d, respectively, for the Glaser and NANO30 sensors. As shown, the sensitivity of the PAC sensor has a peak at about 150 kHz, while the Glaser-type sensor has a nearly flat response from 20 kHz to 1 MHz.

Each of the calibration experiments were repeated five times, and some small differences in the estimated instrument response were observed. When testing in Position 1 and 3, multiple sensors could be tested simultaneously, therefore variations between calibration test results were found to be overwhelmingly due to variations in the calibration source (see Sect. 3.3) rather than in wave propagation effects or instrument response.

The calibration is not valid in any frequency range where the signal to noise ratio (SNR) drops to one. As an illustrative example of the control of SNR over calibration bandwidth, noise spectra are included in Fig. 6b–c. The noise signal, $n(t)$, is a 400 μs segment of the recorded signal taken before the first wave arrival and windowed with the Blackman Harris window. The amplitude of the FT of the noise signals (which are unique for each sensor and data acquisition setup) are shown in Fig. 6b for the Glaser and NANO30 sensors. Noise spectra are obtained by dividing the FT of $n(t)$ by $U_3(\mathbf{x}, \omega)$, and are shown in Fig. 6c. For this capillary fracture test, the SNR drops to 1 at about 1.8 MHz for the NANO30 sensor and at about 4 MHz for the Glaser-type sensor. When the SNR drops to 1, calibration results are certainly not valid. Figure 6c illustrates one of the benefits of the absolute calibration scheme: because the recorded signal was in units of Volts and the theoretical signal was in units of nm, the instrument response function has units of V/nm. Finally, the phase of $\hat{I}(\omega)$ for the two sensors are shown in Fig. 6d. Note that for both sensors, the phase of $\hat{I}(\omega)$ becomes erratic and diverges when the SNR becomes small. This is because phase is undefined when the amplitude is effectively zero.

5.1 Accuracy of Source Models

The accuracy of the source models is explored by comparing $\hat{I}(\omega)$ obtained from calibration tests with different calibration sources. Figure 7 compares $|\hat{I}(\omega)|$ made using two different calibration sources and two different sensor positions. The spikes in $|\hat{I}(\omega)|$ from the ball drop source, at approximately 2.2, 3.3, and 4.4 MHz, are due to the presence of zeros in the spectrum of the 0.40 mm diameter ruby ball impact source model at those frequencies. The ball impact and capillary fracture source models yield $|\hat{I}(\omega)|$ that are in very good agreement at lower frequencies; at higher frequencies (above 500 kHz) the results from the two gradually diverge, indicating that the source models may not be entirely accurate for the estimation of spectral amplitudes in the MHz range (see Sect. 3.3 for a discussion of the variability of the calibration sources). While this calibration approach relies on a number of idealizations, such as the point source and point receiver approximations and the source models of (6) and (7), the close match between the results of ball drop and capillary source calibrations (Fig. 7), demonstrates the validity of the approach.

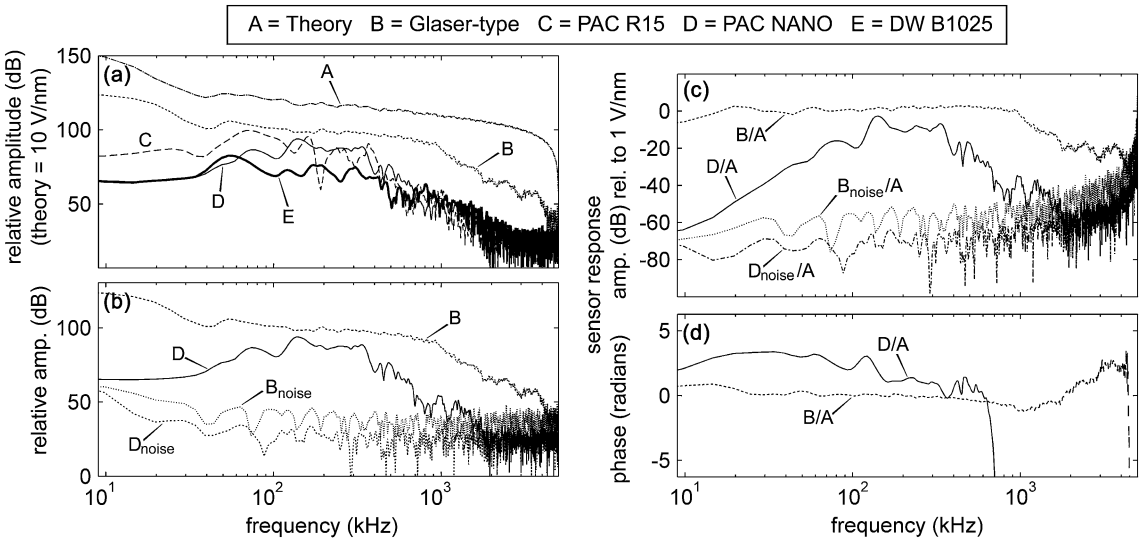

Fig. 6 Spectra for the calculation of the instrument response function in the frequency domain. (**a**) The amplitude of the FT of the five signals shown in Fig. 5, (**b**) the amplitude of the FT of the Glaser-type and PAC NANO30 signal shown alongside the amplitude of the FT of the noise for these two sensors, (**c**) amplitude of $\hat{I}(\omega)$, obtained via spectral ratios, for the Glaser-type and PAC NANO30 sensors are compared to and the amplitude of the respective noise spectra, and (**d**) the phase of $\hat{I}(\omega)$

5.2 Directionality and the Aperture Effect

For many sensors, the instrument response may be a function of the direction of arrival of incoming waves. Here we describe this phenomenon as a directionality effect. Sensor directionality can be estimated from a comparison of $\hat{I}(\omega)$ obtained from tests with different sensor positions, as shown in Fig. 7. Note that a different Green's function must be used for each different sensor position. For the Glaser-type sensor, there is little difference between $|\hat{I}(\omega)|$ obtained from tests in Position 1 and Position 2 (no directionality effect). For the other sensors, instrument response is a function of the direction of arrival of incoming waves. The PAC R15, PAC NAN030, and the DW B1025 sensors have decreased high frequency sensitivity when tested in Position 1 compared to Position 2. While it is difficult to identify the cause of the observed directionality, the finite sensor aperture is the most likely candidate.

Known as the aperture effect (e.g [6]), a decrease in the recorded wave amplitude at high frequencies is due to multiple wavelengths being averaged over the area of contact, or aperture, of a sensor. The aperture effect is maximized in Position 1, where waves arrive tangential to the sensor face, and minimized in Position 2, where the waves arrive normal to the sensor face. Therefore, comparing the results from Position 1 and 2 provides a good way of assessing the aperture effect. The aperture effect is most evident on the DW B1025 and PAC R15 sensors, and the diameter of their piezoelectric elements is large compared to those of PAC NANO30 and Glaser-Type sensors. The nominal area of contact of the DW B1025 sensor has a diameter of 8 mm, which is equal to the wavelength of S waves in steel at 400 kHz. Above this frequency, the results from Position 1 and Position 2 have clearly diverged. Similarly, for the PAC R15 (nominal diameter of 16 mm), significant aperture effects can be seen above 200 kHz, for the PAC NANO30 sensor (5.5 mm diameter) these effects occur above 550 KHz, and for the Glaser-type sensor (0.5 mm diameter) aperture effects occur above 6.4 MHz. In materials with a lower wave speed, such as plastic, the wavelengths at a fixed frequency are somewhat smaller than in steel, therefore the aperture effect will be more significant and will affect a lower frequency band.

In this study, sensors are calibrated against a theoretical displacement time history, therefore $|\hat{I}(\omega)|$ is an estimate of the displacement response spectra. The Glaser-type sensor has a nearly flat response spectrum, therefore it is best described as a displacement sensor in the frequency band of interest. This means that voltage is linearly proportional to surface normal displacements in that frequency band. The DW B1025 sensor has a nearly linear displacement response spectrum with a slope of 1 (20 dB per order of magnitude in frequency), therefore it is best described as a velocity sensor in the same frequency band. A reference line with a slope of 1 is shown in Fig. 7d as a guide for the eye. A perfect fit to this line would indicate a flat velocity response spectrum. The PAC sensors show multiple resonant frequencies and are therefore not easily described as displacement sensors or velocity sensors. Instead, they are sensitive to a combination of displacement, velocity, and acceleration which varies with frequency.

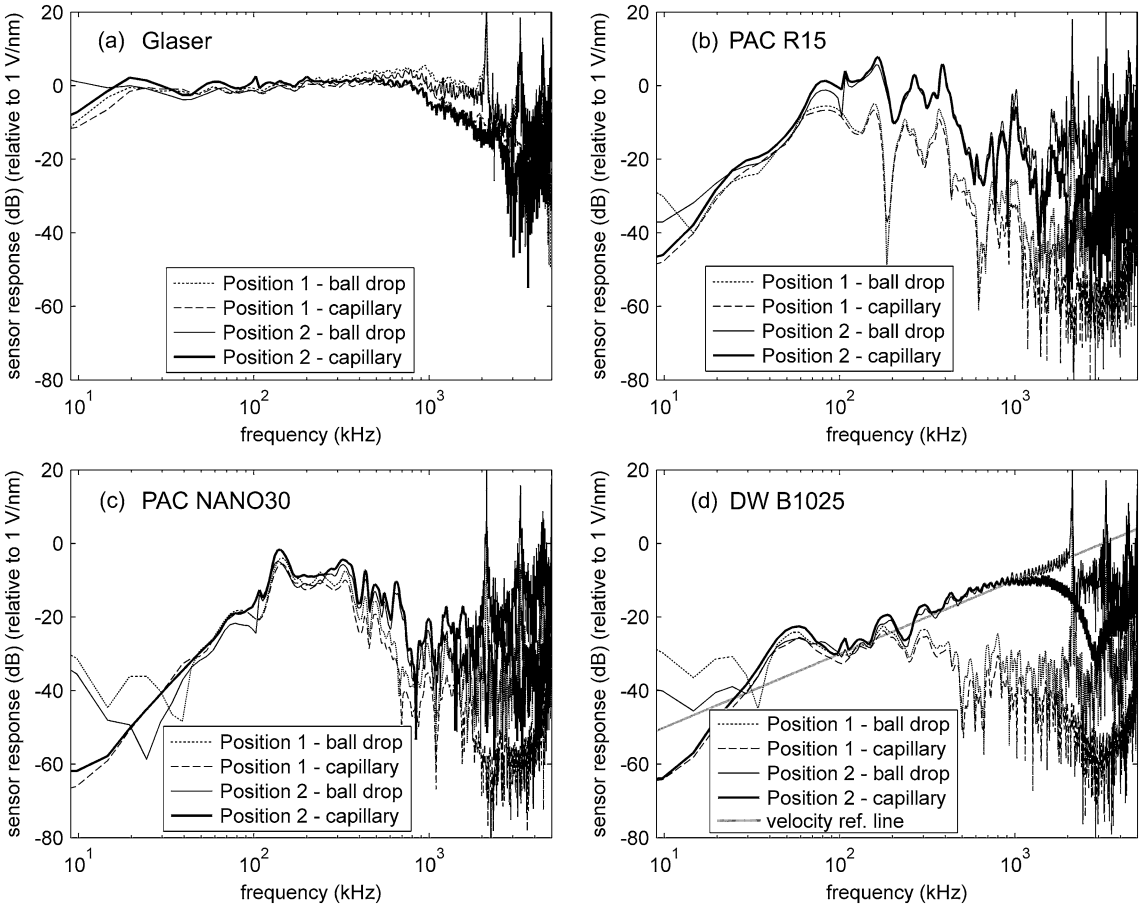

Fig. 7 Calibrations using different combinations of sensor positions ($\mathbf{x}_1$ and $\mathbf{x}_2$) and calibration sources (0.40 mm ruby ball impact and 0.40 mm glass capillary fracture), for the four different sensors tested. Deviation between $|\hat{I}(\omega)|$ from tests using different sensor positions illustrates aperture effects. The similarity between $|\hat{I}(\omega)|$ from tests using different sources verifies the two source models. The reference line shown in (**d**) indicates a flat velocity response spectrum

6 Time Domain Modeling of Instrument Response

The frequency domain methodology described in Sect. 5 requires only spectral division (9), but in that approach, important phase information can be easily lost or distorted due to the influence of noise and windowing. Alternatively, when calculating the sensor response in the time domain (8), phase information is more robustly incorporated into the solution, and this is advantageous when we want to simulate or remove the effects of the sensor, so that a precise displacement time history can be obtained from recorded signals. The main challenges of the time domain approach are the practical issues involved in deconvolution [26]. In order to circumvent many of these problems, we do not directly invert for the instrument response function using (4). Instead, we approximate the sensor response with a time domain model (see for example [27]), and use $u_3(\mathbf{x}, t)$ and $s(\mathbf{x}, t)$ as the input and output, respectively, to estimate the model parameters. For brevity, we consider only one type of model and its usefulness for AE analysis. We chose the commonly-used autoregressive moving average (ARMA) model [27–29] of the form:

$$s(\mathbf{x}, t) = \sum_{k=0}^{n} b_k u_3(\mathbf{x}, t - kT) - \sum_{j=1}^{m} a_j s(\mathbf{x}, t - jT) \qquad (10)$$

where T is the sampling period ($T = 100$ ns, for the examples in this study), and a and b are arrays containing the autoregressive and moving average (convolutional) model parameters, respectively.

A time domain model is a way of representing a system or process (a transfer function) which maps one signal (in this case, $u_3(\mathbf{x}, t)$) to another signal ($s(\mathbf{x}, t)$). The purpose of the current ARMA model is to numerically simulate the distorting effect that the sensor and recording system has on $u_3(\mathbf{x}, t)$ and to allow it to be efficiently removed from an arbitrary $s(\mathbf{x}, t)$. The ARMA model itself will have a response function, referred to here as the ARMA response spectrum in the frequency domain. The ARMA model has much fewer parameters than the number of data points in the $u_3(\mathbf{x}, t)$ and $s(\mathbf{x}, t)$ signals, so the parameters can be estimated using

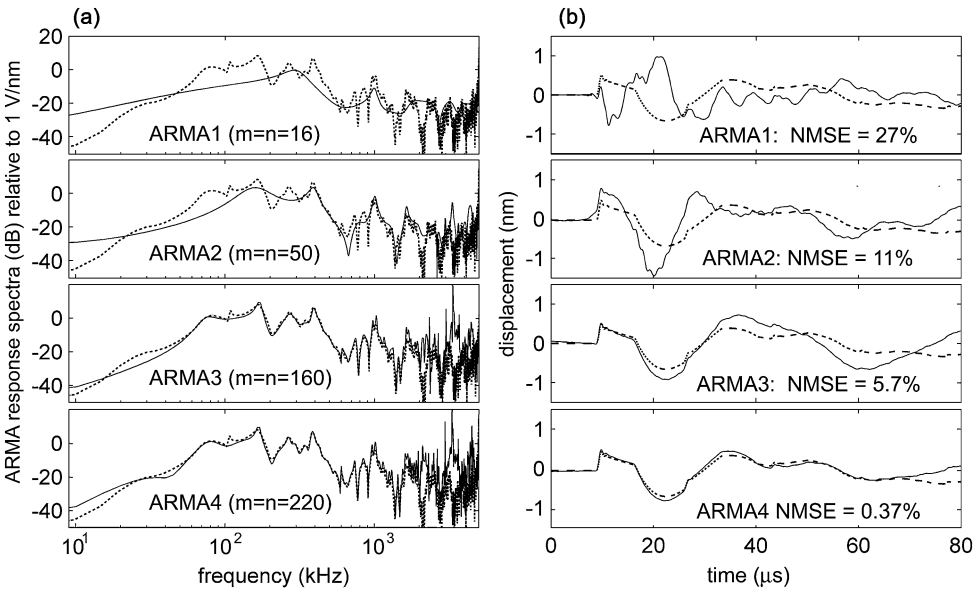

Fig. 8 ARMA model building and validation for the PAC R15 sensor. (**a**) The ARMA response spectra (*solid lines*) are compared to $|\hat{I}(\omega)|$ (*dashed lines*) for four ARMA models with $m = n = 16$, 50, 160, and 220 parameters. A larger number of parameters yields a more detailed ARMA response spectrum. (**b**) Estimates of displacement time history obtained by deconvolving the ARMA response spectrum from $s^{\text{val}}(t)$ are compared to $u^{\text{val}}(t)$ for each of the four ARMA models of increasing complexity. Signals shown in (**b**) have been band passed between 15 kHz and 1 MHz

a least squares formulation. Many criteria exist by which the user can determine the number of parameters (m and n, in (10)) to be included in the ARMA model (i.e. Akaike's information criterion [27]), but ultimately it is a tradeoff between fewer parameters, which decreases the sensitivity of the model to noise and small errors in the Green's function estimates, and more parameters, which allows a more complicated model, and will thus provide a better fit between the ARMA response spectrum and the instrument response spectrum, $\hat{I}(\omega)$. A sensor which has a flat or smoothly varying response spectrum will require only a simple model with few model parameters, while a sensor with a very rough or jagged spectrum will require a more complicated model and more parameters (larger m and n) for the same quality of fit between the ARMA response spectrum and $\hat{I}(\omega)$.

We employ the system identification toolbox of the commercial software *MATLAB* [30] for the determination of ARMA model parameters for each of the four sensors tested. An example of ARMA model building and validation is shown in Fig. 8 for the PAC R15 sensor calibrated in Position 2, using the impact of a 0.40 mm ruby ball dropped 310 mm onto the steel test plate as a calibration source. First, we obtain an input-output pair ($u_3(\mathbf{x}, t)$ and $s(\mathbf{x}, t)$) from the calibration test. Here, we denote these signals as $u^{\text{build}}(t)$ and $s^{\text{build}}(t)$. Then, to illustrate the effect of different model complexity, four different ARMA models ($m = n = 16$, 50, 160, 220) were derived from this pair. We used the "arx" command in *MATLAB* which computes least squares estimates of a and b vectors, given $u^{\text{build}}(t)$ and $s^{\text{build}}(t)$. (For simplicity, we chose only models where $m = n$.) The amplitude of the ARMA response spectra for each of the four models are shown in Fig. 8a. As shown, when the number of parameters of the ARMA model is increased, the ARMA response spectrum becomes more detailed and more closely matches $|\hat{I}(\omega)|$ (Fig. 8a, dashed lines) which was estimated from $u^{\text{build}}(t)$ and $s^{\text{build}}(t)$ following the methodology of Sect. 5.

Once the model parameters have been determined, the ARMA model can be used in a forward sense (as a filter) to simulate the distorting effects of the sensor on an arbitrary displacement time history. This is accomplished by substituting an arbitrary displacement time history for $u_3(\mathbf{x}, t)$ in (10), or by means of the "filter" command in *MATLAB* or equivalent software. Alternatively, the ARMA model can be used in an inverse sense to remove the effects of the sensor from an arbitrary recorded signal, $s(\mathbf{x}, t)$, and obtain an estimate, $\hat{u}(t)$, of the displacement time history, $u_3(\mathbf{x}, t)$, felt by the sensor. The ARMA response spectrum is intended to match $\hat{I}(\omega)$, therefore deconvolving the ARMA response function from any recorded signal will essentially remove the effects of the sensor from that signal. We prefer the ARMA deconvolution method for removing sensor distortion over other methods (e.g. inverse Fourier transforming the result of (9) or calculating $g_{33}(\mathbf{x}, \omega; \boldsymbol{\xi}, \varpi)^{-1}$) because with ARMA deconvolution we divide $S(\mathbf{x}, \omega)$ by the relatively smooth ARMA spectrum rather than by $\hat{I}(\omega)$. Here, we assume $I(\omega)$ is a relatively smooth function and that we have intelligently chosen the ARMA model order so that the ARMA spectrum is detailed enough to capture the general features of $I(\omega)$ but still smoothes over the fine details of $\hat{I}(\omega)$, which are assumed to be the result of noise from $s^{\text{build}}(t)$. To accomplish the ARMA deconvolution, we divide $S(\mathbf{x}, \omega)$ by the ARMA response spectrum, calculated using *MATLAB* "freqz" command, and apply an inverse FT to the result.

Finally, the models are validated with a second input-output pair, denoted $u^{\text{val}}(t)$ and $s^{\text{val}}(t)$, obtained from a second calibration test, this time using a glass capillary frac-

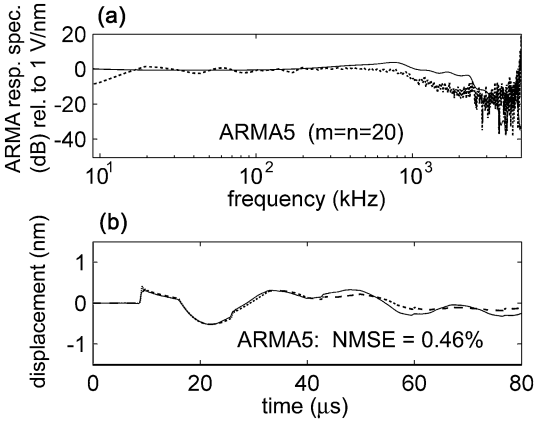

Fig. 9 An example of an ARMA model ($m = n = 20$) intended to mimic the Glaser-type sensor. The model was built with an input-output pair obtained from a calibration test in Position 2, using the impact of a 0.40 mm ruby ball dropped 310 mm onto the steel test plate, and it is validated using an input-output pair obtained from a glass capillary test in the same position

ture as a source. Figure 8b shows a comparison between the theoretical displacement time history, $u^{\text{val}}(t)$ (dashed lines), and displacement time history estimates, $\hat{u}(t)$ (solid lines), obtained by deconvolving the ARMA response spectrum from $s^{\text{val}}(t)$. As the number of parameters of the ARMA model increases, $\hat{u}(t)$ more closely matches $u^{\text{val}}(t)$. In this case, the ARMA model with $m = n = 16$ does a poor job of capturing the complicated response of the PAC R15 sensor. Some improvements are made by increasing the parameters to $m = n = 50$. The third model ($m = n = 160$) does an excellent job of capturing all but the low frequency effects of the PAC R15 sensor, while the fourth model ($m = n = 220$) shows modest improvements over the third. The goal of the ARMA model building is to intelligently choose the ARMA model with the lowest number of parameters whose response spectrum adequately matches $I(\omega)$. The ARMA model can then be used to mimic or remove sensor distortions.

Model error can be quantified with the normalized mean square error (NMSE) [31],

$$NMSE = \frac{1}{p}\sum_{i=1}^{p}\frac{\left(\hat{u}(t+iT) - u^{\text{val}}(t+iT)\right)^2}{u_{\max}^2}, \tag{11}$$

where $u_{\max}$ is the maximum of $u^{\text{val}}(t)$. The four models described in Fig. 8 ($m = n =$ 16, 50, 160, and 220) produced NMSE of 27%, 11%, 5.7%, and 0.37%, respectively. In contrast, the smoothness of the spectrum of the Glaser-type sensor required an ARMA model of only $m = n = 20$ parameters to achieve a NMSE of 0.46%. This model for the Glaser type sensor is shown in Fig. 9.

7 Conclusions

Starting with a description of the theoretical framework for AE and ultrasonic signal analysis, this paper describes how calibration sources and wave propagation effects can be modeled so that the instrument response can be estimated from simple but powerful experiments. The framework and methodology are useful for obtaining absolute amplitudes and displacement time histories from recorded AE signals, but are also designed to be practical for the AE researcher. Unique to this method, two different calibration sources are employed so that the accuracy of both source models can be estimated. Additionally, two different source-sensor orientations were studied, each with unique Green's functions. This allows the effects of directionality, such as the aperture effect, to be evaluated. Results from these calibration studies highlight the differences between the four sensors tested and illustrate some of the ways in which real sensor response deviates from the ideal case. For example, the DW B1025 sensor is well described as a velocity sensor in the 80 kHz to 1 MHz frequency band, but, when waves arrive from low incidence angles, the effect of the 8 mm aperture of the sensor can cause considerable distortions at frequencies above about 300 kHz. In contrast, the Glaser-type sensor is well described as a displacement sensor in the 20 kHz to 1 MHz frequency band, and the 0.5 mm sensor contact area introduces negligible aperture effects. The response of the two PAC sensors is not easily linked to a single physical quantity such as surface velocity or displacement. Instead, multiple resonances in the frequency band of interest cause these sensors to respond to a frequency-dependent mixture of displacement, velocity, and acceleration, which is considerably more complicated to model.

The theoretical framework described in this paper is valid for any frequency band. Experimental constraints are what limit the calibration range to ~50 kHz–~2.0 MHz. At high frequencies, a very strong source is needed to achieve a high SNR because the sensors described tend to lose sensitivity in the MHz range. Additionally, source models ((6) and (7)) may lose accuracy in those high frequency ranges. At low frequencies, long time windows are needed so that many periods are captured within the recorded signal. Long-time Green's functions require the inclusion of reflections from the side edges of the plate, and these additions make the Green's functions more complicated. In this study, Green's functions were calculated for an infinite plate geometry, so the 610 mm square steel test plate restricts time windows to 400 µs. Consequently, there is high uncertainty in spectral estimates below about 50 kHz, where less than 20 periods were captured in the time window.

The frequency domain methods described in Sect. 5 are convenient for estimating the instrument response spectrum, so that the flatness or resonant frequencies of a sensor can

be determined, and different sensors can be compared or classified, but the time domain models of Sect. 6 are more useful for the simulation or removal of sensor effects, because indispensable phase information is "hard-wired" into the solution. The determination of a model which captures the salient features of a sensor's instrument response allows physical quantities (i.e. surface displacements) to be obtained from recorded signals. Building a suitable time domain model to mimic a particular sensor's effects is somewhat of an art. Nevertheless, this study demonstrates that it is possible to build, validate, and quantify the suitability of a given model from the results of simple calibration experiments, even for the more complicated PAC R15 sensor. The calibration techniques described in this paper allow researchers to ascertain the strengths and limitations of instrumentation and the physical meaning of recorded signals—necessary steps toward building reliable and standardized nondestructive evaluation techniques.

Acknowledgements The authors would like to acknowledge constructive reviews by three anonymous reviewers which improved this paper. This work was funded by National Science Foundation grant CMS-0624985.

References

1. Miller, R., McIntire, P.: Nondestructive Testing Handbook Second Edition, vol. 5: Acoustic Emission Testing. American Society for Nondestructive Testing, Columbus (1987)
2. Grosse, C., Ohtsu, M.: Acoustic Emission Testing: Basics for Research—Applications in Civil Engineering; With Contributions by Numerous Experts. Springer, Heidelberg (2008)
3. McLaskey, G., Glaser, S.: Hertzian impact: experimental study of the force pulse and resulting stress waves. J. Acoust. Soc. Am. **128**, 1087–1096 (2010)
4. McLaskey, G., Glaser, S.: Micromechanics of asperity rupture during laboratory stick slip experiments. Geophys. Res. Lett. **38**, L12302 (2011)
5. Hsu, N., Breckenridge, F.: Characterization of acoustic emission sensors. Mater. Eval. **39**, 60–68 (1981)
6. Eitzen, D., Breckenridge, F.: Acoustic emission sensors and their calibration. In: Miller, R., McIntire, P. (eds.) Nondestructive Testing Handbook Second Edition, vol. 5: Acoustic Emission Testing, pp. 121–132. American Society for Nondestructive Testing, Columbus (1987)
7. Hatano, H., Watanabe, T.: Reciprocity calibration of acoustic emission transducers in Rayleigh-wave and longitudinal-wave sound fields. J. Acoust. Soc. Am. **101**, 1450–1455 (1997)
8. Proctor, T.: An improved piezoelectric acoustic emission transducer. J. Acoust. Soc. Am. **71**, 1163–1168 (1982)
9. McLaskey, G., Glaser, S.: High-fidelity conical piezoelectric transducers and finite element models utilized to quantify elastic waves generated from ball collisions. In: Tomizuka, M., Yun, C., Giurgiutiu, V. (eds.) Proc. SPIE, vol. 7292, pp. 72920S-1–72920S-18 (2009)
10. Sansalone, M., Street, W.: Impact Echo: Nondestructive Evaluation of Concrete and Masonry. Bulbrier Press, Ithaca (1997)
11. Hsu, N., Simmons, J., Hardy, S.: An approach to acoustic emission signal analysis—theory and experiment. Mater. Eval. **35**, 100–106 (1977)
12. Stump, B., Johnson, L.: The determination of source properties by the linear inversion of seismograms. Bull. Seismol. Soc. Am. **67**, 1489–1502 (1977)
13. Aki, K., Richards, P.: Quantitative Seismology: Theory and Methods. Freeman, San Francisco (1980), Chapter 4
14. To, A., Glaser, S.: Full waveform inversion of a 3-D source inside an artificial rock. J. Sound Vib. **285**, 835–857 (2005)
15. Oppenheim, A., Schafer, R.: Discrete Time Signal Processing, 2nd edn. Prentice Hall, New Jersey (1999)
16. Breckenridge, F., Proctor, T., Hsu, N., Fick, S., Eitzen, D.: Transient sources for acoustic emission work. In: Yamaguchi, K., Takahashi, H., Niitsuma, H. (eds.) Progress in Acoustic Emission V, pp. 20–37. The Japanese Society for NDI, Sendai (1990)
17. Hsu, N.: Acoustic emission simulator, U.S. Patent No. 4018084 (1977)
18. Breckenridge, F., Tscheigg, C., Greenspan, M.: Acoustic emission: some applications of Lamb's Problem. J. Acoust. Soc. Am. **57**, 626–631 (1975)
19. Goldsmith, W.: Impact. Dover, New York (2001)
20. Scruby, C., Drain, L.: Laser Ultrasonics: Techniques and Applications. Taylor & Francis, London (1990)
21. White, J.: Seismic Waves: Radiation, Transmission, and Attenuation. McGraw-Hill, New York (1965)
22. Johnson, L.: Green's function for Lamb's problem. Geophys. J. R. Astron. Soc. **37**, 99–131 (1974)
23. Hsu, N.: Dynamic Green's functions of an infinite plate—a computer program. Technical Report No. NBSIR 85-3234, National Bureau of Standards, Center for Manufacturing Engineering, Gaithersburg, MD (1985)
24. Pekeris, C.: The seismic surface pulse. Proc. Natl. Acad. Sci. **41**, 469–480 (1955)
25. Knopoff, L.: Surface motions of a thick plate. J. Appl. Phys. **29**, 661–670 (1958)
26. Michaels, J.: Fundamentals of deconvolution with applications to ultrasonics and acoustic emission. MS thesis, Cornell University, Ithaca (1982)
27. Shumway, R., Stoffer, D.: Time Series Analysis and Its Applications. Springer, New York (2006)
28. Ljung, L.: System Identification: Theory for the User. Prentice-Hall, Englewood Cliffs (1987)
29. Marple, S. Jr., Lawrence, S.: Digital Spectral Analysis with Applications. Prentice-Hall, Englewood Cliffs (1987)
30. Ljung, L.: System Identification Toolbox, for Use with Matlab. The Mathworks, Natick (2006)
31. Baise, L., Glaser, S., Sugano, T.: Consistency of dynamic site response at port island. Earthquake Eng. Struct. Dyn. **30**, 803–818 (2001)